ACS APPLIED MATERIALS & INTERFACES

Research Article

www.acsami.org

In-Situ Fabrication of a Self-Aligned Selective Emitter Silicon Solar Cell Using the Gold Top Contacts To Facilitate the Synthesis of a Nanostructured Black Silicon Antireflective Layer Instead of an External Metal Nanoparticle Catalyst

Yen-Tien Lu[†] and Andrew R. Barron*[,‡,§,∥]

[†]Department of Chemical and Biomolecular Engineering, Rice University, 6100 Main Street, Houston, Texas 77005, United States

[‡]Department of Chemistry, Rice University, 6100 Main Street, Houston, Texas 77005, United States

[§]Department of Materials Science and NanoEngineering, Rice University, 6100 Main Street, Houston, Texas 77005, United States

[∥]Energy Safety Research Institute, College of Engineering, Swansea University, Singleton Park, Swansea SA2 8PP, Wales, United Kingdom

Supporting Information

ABSTRACT: Silicon solar cells with nanopore-type black silicon (b-Si) antireflection (AR) layers and self-aligned selective emitter (SE) are reported in which the b-Si structure is prepared without the traditional addition of a nanoparticle (NP) catalyst. The contact-assisted chemical etching (CACE) method is reported here for the first time, in which the metal top contacts on silicon solar cell surfaces function as the catalysts for b-Si fabrication and the whole etching process can be done in minutes at room temperature. The CACE method is based on the metal-assisted chemical etching (MACE) solution but without or metal precursor in the Si etchant ($HF:H_2O_2:H_2O$), and the Au top contacts, or catalysts, are not removed from the solar cell surface after the etching. The effects of etching time, HF and H_2O_2 concentration, and the $HF:H_2O_2$ ratio on the b-Si morphology, surface reflectivity, and solar cell efficiency have been investigated. Higher [HF] and [H_2O_2] with longer etching time cause collapse of the b-Si nanoporous structure and penetration of the p−n junctions, which are detrimental to the solar cell efficiency. The b-Si solar cell fabricated with the $HF:H_2O_2:H_2O$ volume ratio of 3:3:20 and a 3 min etch time shows the highest efficiency 8.99% along with a decrease of reflectivity from 36.1% to 12.6% compared to that of the nonetched Si solar cell.

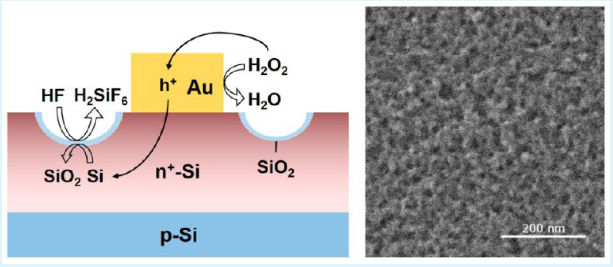

KEYWORDS: *black silicon, solar cell, contact, antireflection, porous, selective emitter*

1. INTRODUCTION

The improved performance approaches of increased efficiency and/or significant reduction of the cost of manufacture are two keys to solar energy achieving grid parity with energy derived from fossil fuels.[1] One of the requirements for an efficient solar cell is low surface reflectivity to maximize the amount of incident photons absorbed by the cell. In the industry, silicon nitride antireflection (AR) coatings based on quarter-wavelength principle are usually deposited on Si wafer surfaces to suppress the surface reflectivity; however, their AR ability is limited since the AR coatings only perform well in a narrow range of light wavelength and incident angles.[2−6]

An alternate material called "black Si" (b-Si) consisting of nanopores or nanowires has been developed because it can overcome the disadvantages of conventional AR coatings. B-Si possesses a gradient change of refractive index between the Si wafer surface and air allowing b-Si to more effectively suppress the reflection on the Si solar cell regardless of the changes in the incident angle and wavelength of the light. The techniques for fabricating b-Si includes reactive ion etching,[7−13] laser irradiation,[14−18] electrochemical etching,[19−22] and metal-assisted chemical etching (MACE).[23−33] Among all of these techniques, the MACE method is the most popular because it has lower energy consumption and needs no complicated instruments. Due to these factors, the MACE method has the potential to be more easily introduced into the current production lines of Si solar cells.[1]

The typical MACE method includes two different steps: deposition of a metal catalyst and electroless chemical etching, respectively. Recently, we have successfully merged the two steps into a one-step reaction in order to further decrease the fabrication cost of b-Si through the use of silver and copper precursors in the Si etchants to produce metal nanoparticle (NP) catalysts.[29,33] As is common with all MACE systems,[24] the metal NPs catalyze the Si wafer oxidation (to SiO_2), which is then etched by the HF (in the etchant solution) to form a porous b-Si

Received: February 2, 2015
Accepted: May 13, 2015
Published: May 13, 2015

DOI: 10.1021/acsami.5b01008
ACS Appl. Mater. Interfaces 2015, 7, 11802−11814

structure. Along with Ag and Cu, Au may also be used as the catalyst.[26,34,35] In fact, Branz et al. first fabricated b-Si by using a one-step Au-assisted chemical etching method with a reagent solution consisting of $HF/H_2O_2/H_2O/HAuCl_4$.[26]

Although the b-Si fabrication processes with different metal catalysts have been successfully demonstrated, the step of removing metal catalysts from the Si wafer surface is still unavoidable for all types of MACE methods.[24] The residual metal catalysts on the solar cell surface can potentially interfere with the cell performance. However, the extra step of metal removal in the b-Si fabrication process not only increases the b-Si fabrication cost but also appears to cause damage to the b-Si structures when the structure is extremely porous.[29,33]

One issue with traditional Si solar cells is the need for not only a lightly doped (10^{18}–10^{19} cm^{-3}) emitter region for photon collection but also a highly doped (10^{20}–10^{21} cm^{-3}) region for the top contact metallization. One solution is a selective emitter (SE) device, which allows more electrons to be collected by the metal contacts and generates a higher open circuit voltage (V_{oc}) and a higher short circuit current density (J_{sc}). Several fabrication techniques for SE Si solar cells have been developed including etch-back emitter,[36,37] laser-doped SE,[38−40] ion implantation process,[41,42] and screen-printable ink.[43,44] These methods typically require 1−3 extra main fabrication steps compared to the conventional Si cell fabrication. Recently, Um et al. have shown that b-Si layers can be formed for a SE Si solar cell by using Ag NPs in the MACE method;[45] however, as noted the complete removal of the residual metal catalyst in the MACE process can be problematic and represents an additional process step.[24,29,33] Furthermore, the cost of the catalyst must be taken into account when considering the application of b-Si.

In order to obviate the need for the metal removal step, we report the fabrication of b-Si on the Si solar cell surface without any addition of metal or metal precursor as catalysts. This unique approach can be considered as a metal-less MACE process in which the Au top contacts assist the Si etching to create the nanoporous surface. Although the fabrication of a porous Si surface by using Au films with an external power supplier has been studied before,[46,47] using Au contacts of Si solar cells to directly fabricate b-Si AR layers on the cell surfaces with electroless chemical etching has not yet been reported. Hence, we have designated this new and energy-saving approach as contact-assisted chemical etching (CACE).

2. EXPERIMENTAL METHODS

There were 4-in. polished single crystalline (100) p-type boron-doped Si wafers (Silicon Quest International), with a bulk resistivity in the range 1−5 Ωcm, used as a bulk Si material for the b-Si solar cells. Isopropyl alcohol (>99.5%, J. T. Baker), PV-381 Aluminum Photovoltaic Metallization Paste (DuPont), buffer oxide etchant (BOE, Transene Company), poly(methyl methacrylate) (PMMA, average MW ∼ 996 000, Sigma-Aldrich), toluene (>99.9%, Sigma-Aldrich), HF (48%, Sigma-Aldrich), H_2O_2 (30%, EMD), and trimethylaluminum (TMA, electronic grade, Sigma-Aldrich) were used as received. Concentrations of metal impurities in the sealed chemicals, which might affect the Si etching, were characterized by Evans Analytical Group or provided by the chemical companies with ICP-AES. Supporting Information Table S1 shows the concentrations of copper, silver, and gold in each chemical.

2.1. Preparation of b-Si Solar Cells. In order to generate p−n junctions in Si wafers, emitter diffusion was performed in a horizontal tube diffusion furnace equipped with 8 in. diameter quartz tubes. The wafers were loaded at a rate of 6 in./min into the tube maintained at 700 °C under N_2 flow. Once the wafers were fully loaded into the tube, the temperature was then ramped to 970 °C under N_2 flow over 20 min. The wafers were then held for 5 min at 970 °C in a flow of 4 Lpm N_2 and 200 sccm O_2. A phosphorus dopant was introduced in the tube by bubbling 690 sccm N_2 through a volume of $POCl_3$ maintained at 18 °C for 70 min. At the end of the 20 min phosphorus doping vapor flow step, the $POCl_3$ bubbler flow was turned off, and a flow of 7 Lpm N_2 and 800 sccm O_2 was maintained in the tube for 70 min as the drive-in step. The tube was then returned to pure N_2 flow and allowed to cool for 10 min during a cool-down step prior to unloading the wafers. This yielded an n-type phosphorus diffusion with a very low sheet resistivity of less than 10 Ω/sq.

Following the diffusion, an aluminum mixture composed of isopropyl alcohol and aluminum paste as 1:1 in weight was spread on the back side of the wafers to form back contacts. The wafers were then fired in a rapid thermal process with a peak temperature of 810 °C and cooled down to the room temperature. The final wafers had a heavily doped n-type front emitter and a heavily doped p-type back surface field.

After the Al metallization, the Si wafers were cut into small pieces with 2 × 2 cm^2 and rinsed with deionized (DI) H_2O, acetone, and DI H_2O sequentially. A 5% PMMA/toluene mixture was spread on the as-formed Al back contact layer as a protection layer, and then the wafers were heated to 180 °C for 20 min to evaporate the toluene solvent. The PMMA layer could prevent the back contact from being etched by the following phosphosilicate glass (PSG) removal and the b-Si etching steps. Next, the Si wafers were immersed into the BOE for 3 min to remove a light blue layer of PSG that resulted from the previous phosphorus diffusion step on the Si wafer surface.

Sputtering was used to deposit Au lines with thickness of 100 nm on the Si wafers. A stainless steel mask with a designed pattern of one busbar and nine fingers was put on the front side of the Si wafers before the sputtering. Supporting Information Figure S1 shows the mask design used for the sputtering. The lengths of both busbar and fingers were 1.8 cm, and the widths of busbar and the fingers were 0.1 cm and 100 μm, respectively. The distance between each finger was 0.2 cm. After sputtering, the wafers were annealed at 180 °C for 1 h to improve the adhesion of Au lines on the wafers.

The Au-deposited Si pieces were then etched in Si etchants that consist of HF (48%), H_2O_2 (30%), and DI H_2O in different $HF:H_2O_2:H_2O$ volume ratios with an equal volume of DI H_2O in sealed plasticware at room temperature. In the text, the volume ratio is given as *X*:*Y*:*Z* corresponding to the volume ratio of HF, H_2O_2, and H_2O in the etchant before the equal volume of DI H_2O is added. There were two categories of etchant compositions investigated in the content, and the $HF:H_2O_2:H_2O$ volume ratios of these two categories were 1:5:*Z* and *X*:*Y*:20, respectively. The 1:5:*Z* category included the 1:5:2, 1:5:5, and 1:5:20 series, and the X:Y:20 category included the ratio as the 1:5:20, 2:4:20, 3:3:20, and 4:2:20 series (Supporting Information Table S2). After etching for the allotted time, the samples were rinsed by DI H_2O and immersed into toluene to remove the PMMA protection layer on the backside of the Si wafer.

In order to maximize the b-Si solar cell efficiency, an Al_2O_3 passivation layer with thickness of 22 nm was deposited on the solar cell surface by atomic layer deposition (ALD). The precursors of Al_2O_3 were DI H_2O and TMA, and the deposition temperature was 200 °C. The wafers were then annealed at 465 °C for 30 min with atmosphere consisting of 80% N_2 and 20% O_2. After annealing, the b-Si solar cells were successfully fabricated.

2.2. Characterization. Scanning electron microscopy (SEM) images were carried out with FEI Quanta 400 by placing samples on double-sided carbon tape that was fixed to aluminum SEM stubs. Images were acquired at a typical operating voltage of 20 kV, with a working distance of 10 mm, spot size 3 in Hi-VAC mode. Before SEM images were taken, the samples were cleaned by canned air to remove dust or tiny particles from the wafer surface.

The total reflectance spectra of the b-Si solar cells were measured with Ocean Optics ISP-REF integrating sphere with internal tungsten light source. The integrating sphere worked in collaboration with a homemade low reflectivity enclosure as a 0% standard and Labsphere SRS-10−010 Reflectance Standard as a 10% standard. The calculated average reflectivity is weighted by the AM1.5 solar spectrum. The average is the integral of the measured reflectivity over the wavelengths

DOI: 10.1021/acsami.5b01008
ACS Appl. Mater. Interfaces 2015, 7, 11802−11814

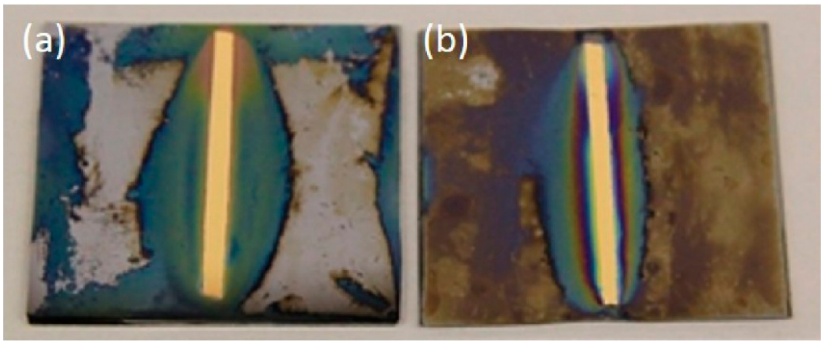

Figure 1. Images of b-Si after the etching treatment. (a) Au-coated Si wafer etched with a Si etchant of $HF:H_2O_2:H_2O$ = 3:3:20 for 3 min. (b) Au-coated Si wafer etched with a Si etchant of $HF:H_2O_2:H_2O$ = 3:3:20 for 3 min with additional 5 μM $AgNO_3$.

from 400 to 1000 nm times the ratio of the solar spectrum at different wavelength divided by the integral of the solar spectrum.

The efficiencies of the b-Si solar cells were calculated from the *I*–*V* curves detected via Keithley 2420 and 2425 High-Current SourceMeter with an Oriel Model 81190 Solar simulator, including light intensity feedback control. The intensity of incident light was 100 mW/cm^2, which was calibrated by an OAI Monosilicon 2 cm × 2 cm reference cell with a BK7 window. The cell was calibrated through NREL's Device Performance Measurements laboratory. The *I*–*V* curve measurement was based on a 4-point probes method in order to get more accurate values. The solar cells were fixed on a metal vacuum chuck that also functioned as two of four probes and connected the back contact of solar cells. On the top surface of solar cells, there were two Cu wires connected to the Au busbar as the remaining two probes. One of them only measured the current and another one only measured the voltage to obtain the real voltage at the solar cell surface.

3. RESULTS AND DISCUSSION

3.1. Mechanism of b-Si Formation Catalyzed by Au Top Contacts. The main issue associated with traditional Ag top contacts prepared with a thermal evaporation step on the Si solar cell surface is that the Ag contacts easily spall from the wafer during etching. As part of a study into whether b-Si can be successfully fabricated during different steps of a fabrication process, Au-coated Si wafers were used and subjected to a typical one-step MACE process with Ag NP precursor ($AgNO_3$/HF/H_2O_2/H_2O).[29] In order to ascertain the influence of the Au contact, an identical sample was exposed to the same HF/H_2O_2/H_2O etchant in the absence of $AgNO_3$. Figure 1 shows optical images of the Au-coated Si solar cells etched with and without addition of $AgNO_3$. As can be seen from Figure 1b, the surface of a sample etched with $AgNO_3$ is entirely etched to show a brown color and also has a relatively uniform etching level compared to the sample etched without $AgNO_3$ (Figure 1a). The Ag precursor in the Si etchant (i.e., $AgNO_3$) is reduced to Ag NPs which are uniformly distributed on the Si wafer and assist the Si etching on the whole wafer surface. However, while b-Si is produced without $AgNO_3$, the wafer only shows significant etching within 4 mm of the Au contact (Figure 1a). The etching occurring around the Au contacts indicates that the predeposited Au contacts are having an intimate effect on the Si etching. We note that the etching also occurs at the wafer edges because of the defects resulting from cutting. When cutting a larger Si wafer into smaller pieces, some defects are generated around the newly formed wafer edges. Since these defects lead to more dangling bonds which are subjected to the Si oxidation more easily, the significant Si etching is also observable around the wafer edges.

Another observation that needs to be mentioned is that the cell etched without $AgNO_3$ (Figure 1a) shows the widest lateral etching distance around the middle part of the Au contact, which gradually becomes narrower along the contact. The reason is that the etching on the wafer surface near the middle part of the contact is catalyzed by whole parts of the Au contact with different levels, so the etching can extend farther from the Au contact. However, for the surface regions, which are closer to the Au contacts ends, since the Si oxidization is less catalyzed by the farther parts of the contact, a narrower etching distance occurs. For the solar cell etched with $AgNO_3$ (Figure 1b), the lateral etching distance does not significantly vary along the Au contact because the etching on the whole cell surface is uniformly catalyzed by the Ag NPs on the cell surface, except the regions which are extremely close to the Au contact.

Figure 2 shows SEM images of the etched regions of the Au-coated Si samples etched with and without $AgNO_3$ shown in Figure 1. The SEM analysis shows that the etched region of the sample etched without $AgNO_3$ (Figure 2a) is consistent with a typical b-Si structure, but its nanopores are smaller than those of the sample etched with $AgNO_3$ (Figure 2b). The sample fabricated with $AgNO_3$ has larger nanopores because the Ag NPs formed on the wafer surface can directly assist the oxidation of Si under the NPs. Hence, the Si etching rate can be more effectively increased to generate larger nanopores on the Si wafer surface.

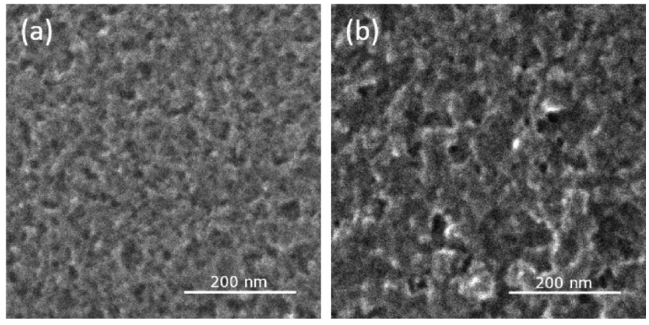

Figure 2. Surface SEM image of b-Si after the Si etching treatment. (a) Surface SEM image of the Au-coated Si wafer etched with an Si etchant of $HF:H_2O_2:H_2O$ = 3:3:20 for 3 min. (b) Surface SEM image of the Au-coated Si wafer etched with an Si etchant of $HF:H_2O_2:H_2O$ = 3:3:20 for 3 min with additional 5 μM $AgNO_3$.

Analysis of the etchant solution by ICP-AES shows that the metal concentrations in the used chemicals associated with the MACE processes are below the detection limits (Supporting Information Table S1). In a comparison with our prior work on fabricating b-Si with Ag and Cu NPs,[29,33] since the metal concentrations in the chemicals are much lower than the lowest

DOI: 10.1021/acsami.5b01008
ACS Appl. Mater. Interfaces 2015, 7, 11802–11814

concentrations we used for b-Si fabrication, we can infer that the Au contacts on the Si wafer surfaces are catalysts of the b-Si formation since the concentrations of other metals in the Si etchant are very low.

An etching mechanism of the CACE method based on the working principle of galvanic cells is proposed to explain the electroless chemical etching with the assistance of Au contacts. A schematic illustration of the proposed process for the formation of a porous structure on the Si wafer surface is shown in Figure 3.

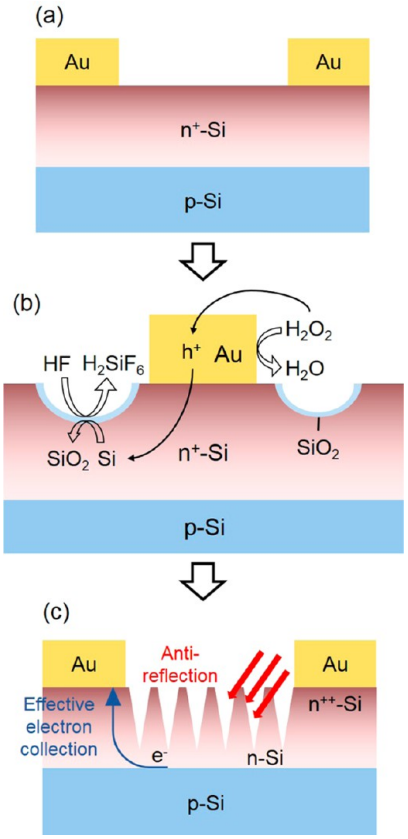

Figure 3. Schematic illustration of the proposed formation process of b-Si structure on the Si wafer surface during the CACE method: (a) Si wafer surface before, (b) during, and (c) after etching.

The Si etching mechanism consists of two half reactions: H_2O_2 reduction and Si oxidation. Since Au has a higher electronegativity than Si, Au can withdraw electrons from the nearby Si wafer surface to the H_2O_2 in the etchant, or inject holes from the H_2O_2 into the nearby Si. Hence, the H_2O_2 is reduced to H_2O at the Au contact surfaces, and the Si wafer regions near the Au contacts are oxidized to SiO_2 (the observed distance effect) which is etched by HF to generate a nanopore-type b-Si structure (Figure 3b). As is observed experimentally there is no etching of the Si regions covered by the Au contacts since this Si does not contact the etchant directly. Furthermore, the Si etching is limited to a distance from the metal controlled by the hole diffusion through the wafer surface that corresponds to our observation in Figure 1.

In order to increase the Si etching uniformity on the solar cell surfaces, the mask mentioned in the Experimental Methods section is used to fabricate a busbar and fingers on the Si solar cell surfaces for the following experiences. Supporting Information Figure S2 shows optical images of the Si solar cells with the Au busbar and fingers without addition of $AgNO_3$. As can be seen in Supporting Information Figure S2, the b-Si solar cell with the Au busbar and fingers has a very uniform etching level on the cell surface although no $AgNO_3$ is added into the Si etchant. After etching, analysis of the b-Si solar cell surface by XPS shows no Au particles are formed on the b-Si surface since no Au atoms are detected on the cell surface not covered by the contacts (Supporting Information Table S3).

On the basis of these results, we proposed that it would be possible to concurrently fabricate a self-aligned SE Si solar cell with a patterned b-Si AR layer on the solar cell surface. In such a process, the initial p-type Si wafers are n-doped by phosphorus diffusion so the wafer surfaces have a higher dopant concentration than the deeper p−n junction region. The metallization followed by non-metal-containing etchants would result in the top Si wafer surface being etched away by the etchant, to reveal the deeper Si. The newly emerging bulk Si surface has a lower dopant concentration and is less conductive compared to the Si regions under the Au contacts, which still possess the original high dopant concentration and build up SEs in the cell as shown in Figure 3c. As noted in the Introduction, Um et al. have concurrently produced b-Si structure and SE on Si solar cell surfaces but based on the MACE method, which involved two extra steps of addition and removal of the metal catalysts.[44] A comparison of etching mechanisms between the CACE method with the MACE method with Ag NPs is shown in Supporting Information Figure S3.

3.2. Fabrication of a Nonetched Si Solar Cell. Before any Si etching treatment, the Au-coated Si solar cells possess a smooth top surface. Figure 4 shows the surface morphology of a nonetched Si solar cell. As can be seen in Figure 4, no nanopores or porous Si structures are found on the wafer surface either from the top-view or cross-sectional images. In order to understand how an Al_2O_3 passivation layer on a Si solar cell affects the surface recombination velocity of charge, a passivation layer (22 nm) was deposited on nonetched Au-coated Si solar cell by ALD first. Table 1 shows the properties of a nonetched solar cell before and after the ALD passivation treatment. After ALD, the solar cell efficiency slightly increases from 5.41% to 5.88%, and V_{oc} and J_{sc}

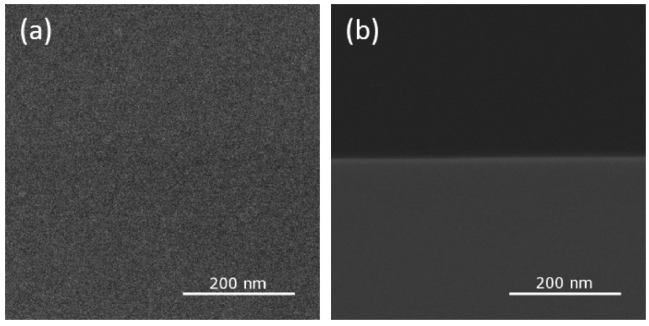

Figure 4. SEM images of nonetched Si solar cell before the ALD passivation treatment: (a) surface SEM image and (b) cross-sectional SEM image.

Table 1. Summary of Properties for the Nonetched Si Solar Cell

Al_2O_3 layer by ALD	efficiency (%)	FF	V_{oc} (V)	J_{sc} (mA/cm^2)	reflectivity
before	5.41	0.73	0.561	13.2	0.446
after	5.88	0.74	0.565	14.1	0.361

DOI: 10.1021/acsami.5b01008
ACS Appl. Mater. Interfaces 2015, 7, 11802−11814

increase from 0.561 to 0.565 V and 13.2 to 14.1 mA/cm^2, respectively. However, the results are not strong enough to prove that the Al_2O_3 passivation layer indeed suppresses the surface recombination velocity of charge carries for the unetched solar cell. The higher efficiency of the solar cell might result from the decrease of surface reflectivity, which drops from 0.466 to 0.361 after ALD.

A possible reason that the surface reflectivity of a solar cell decreases after Al_2O_3 passivation layer is deposited by ALD is that it has an intermediate refractive index (1.8) between that of the air (1.0) and the smooth Si wafer surface (3.5). The intermediate refractive index allows the passivation layer to function like an AR coating layer even though the layer thickness is not thick enough to significantly suppress the reflection on the cell surface. More observations related to the Al_2O_3 passivation layers will be discussed below.

We have investigated the effects of etchant concentrations and the properties of the resulting b-Si solar cells. In order to discuss the results more easily, the results are divided into two different categories based on the HF:H_2O_2:H_2O volume ratio in the Si etchants.

3.3. Effects of HF and H_2O_2 Concentrations on b-Si Solar Cell Fabrication. By using the Si etchant consisting of the highest [HF] and [H_2O_2], HF:H_2O_2:H_2O = 1:5:2, the fabricated b-Si solar cells possess the longest nanopores among all the samples, which corresponds with our previous work.[29] A higher [H_2O_2] accelerates the oxidation rate of Si to SiO_2, and a higher [HF] increases the etching rate of the as-formed SiO_2; both are beneficial for nanopore growth on the Si wafer surface.

Figure 5 shows SEM images of b-Si solar cells fabricated with a HF:H_2O_2:H_2O volume ratio = 1:5:2. After 5 min of etching, the fabricated nanopores, which have maximum diameter around 50 nm and length around 950 nm, can be clearly observed on the wafer surface (Figure 5a,b). It should be mentioned that the top parts of the nanopores are very porous; as a consequence, the outlines of the nanopore tips cannot be clearly seen in the cross-sectional SEM image (Figure 4b).

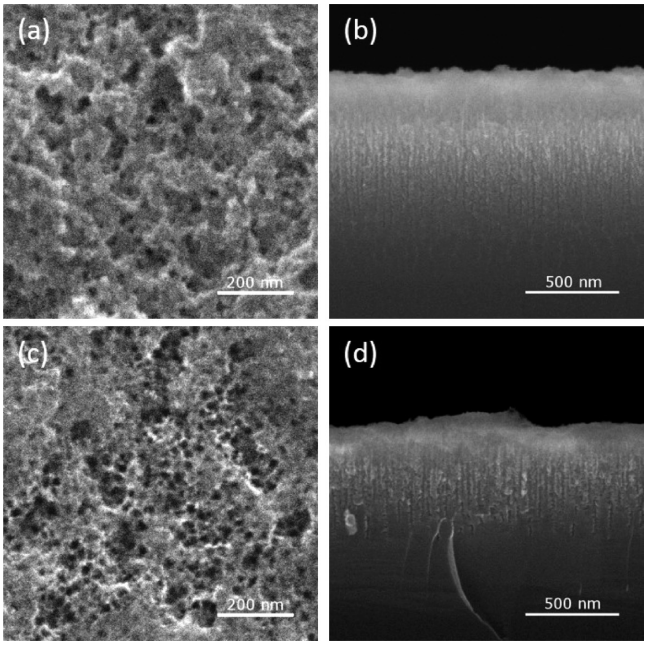

Figure 5. Surface and cross-sectional SEM images of b-Si solar cells fabricated with a HF:H_2O_2:H_2O volume ratio = 1:5:2 for 5 min (a, b) and 10 min (c, d).

As the etching time increases to 10 min, more nanopores are appearing on the wafer surface, and the maximum diameter of nanopores increases to 80 nm (Figure 5c). However, this higher density of nanopore population also causes an extremely porous surface which will easily collapse and result in the shorter nanopores, 750 nm (Figure 5d). From the cross-sectional SEM image, the wafer surface becomes much rougher, and only nanopores with clearer outlines still exist, which indicates that the majority of extremely porous parts of the nanopores have collapsed and have been removed from the wafer surface.

In general, using a lower [HF] and [H_2O_2] for Si etching, such as the HF:H_2O_2:H_2O ratios of 1:5:5 and 1:5:20, causes the b-Si structures to possess smaller nanopore sizes compared to those etched with the 1:5:2 ratio due to the slower etching rate. Figure 6 shows the SEM images of b-Si solar cells etched with the HF:H_2O_2:H_2O volume ratio = 1:5:5. After etching for 3 min, small and short nanopores with maximum diameters of 30 nm and length of 240 nm are observed on the wafer surface (Figure 6a,b). As the etching time increases to 5 min, the nanopores become extremely porous, and the maximum nanopore size grows to 60 nm in diameter and 450 nm in length (Figure 6c,d). However, the nanopore size is still smaller than that of the b-Si fabricated with the ratio as 1:5:2 with the same etching time (50 nm in diameter and 950 nm in length).

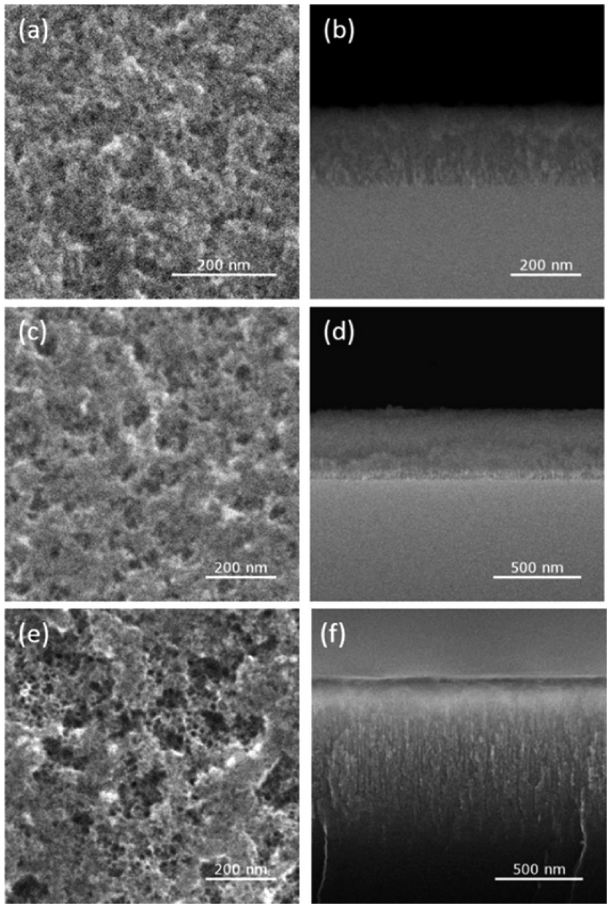

Figure 6. Surface and cross-sectional SEM images of b-Si solar cells fabricated with a HF:H_2O_2:H_2O volume ratio = 1:5:5 for 3 min (a, b), 5 min (c, d), and 10 min (e, f).

DOI: 10.1021/acsami.5b01008
ACS Appl. Mater. Interfaces 2015, 7, 11802−11814

Interestingly, after 10 min of etching, the maximum nanopore diameter and length keep increasing to 85 and 850 nm, respectively (Figure 6e, f), which are slightly larger and longer than the nanopores fabricated with the higher [HF] and [H_2O_2], or HF:H_2O_2:H_2O = 1:5:2. Even though the b-Si structures slightly collapse on the wafer surface, the remaining nanopores are still long enough to make the collapses less significant and the wafer surface relatively smooth. Thus, the use of lower [HF] and [H_2O_2] can effectively prevent excessively aggressive etching which may cause the serious collapse of b-Si structure.

The nanopore size in the b-Si decreases further when [HF] and [H_2O_2] are lowered. With a ratio of HF:H_2O_2:H_2O = 1:5:20, the Si etching is significantly suppressed, leading to a low population density of nanopores on the Si wafer surface after 5 min of etching. Figure 7 shows the SEM images of b-Si solar cells

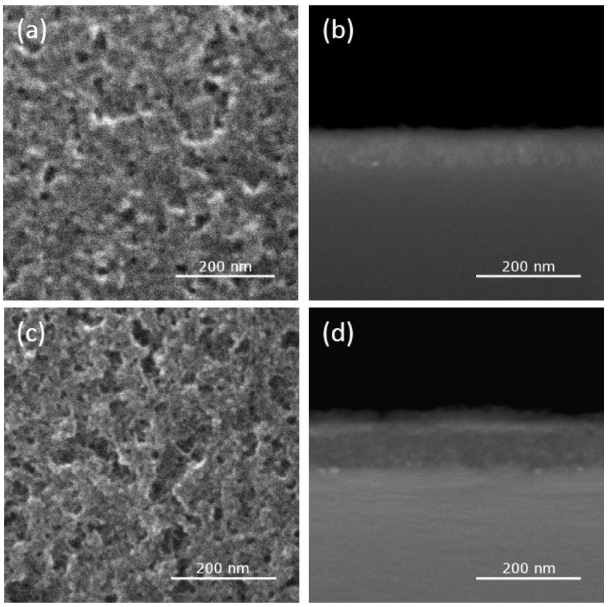

Figure 7. Surface and cross-sectional SEM images of b-Si solar cells fabricated with a HF:H_2O_2:H_2O volume ratio = 1:5:20 for 5 min (a, b) and 10 min (c, d).

fabricated with a HF:H_2O_2:H_2O volume ratio = 1:5:20. As seen in Figure 7, the maximum nanopore diameter (45 nm) and length (100 nm) are also extremely small. As the etching time is increased to 10 min, the maximum nanopore diameter and length only increase to 70 and 130 nm, respectively (Figure 7c,d). In a comparison with the growth rate for the b-Si fabricated with the ratios of 1:5:2 and 1:5:5, the nanopore growth rate is much slower due to the lower [HF] and [H_2O_2] used. Hence, the lack of nanopore collapse observed on the wafer surface looks more obvious since this b-Si has a shorter length.

The surface morphology of b-Si solar cells has direct effects on AR ability and energy conversion efficiency of solar cells. The working principle of the b-Si AR layers is based on the gradient change of the refractive index of b-Si on the wafer surface. Table 2 shows the summary of properties of all b-Si solar cells reported herein. A plot of the reflectivity of b-Si solar cells fabricated with the etchant ratio of 1:5:*Z* is shown in Figure 8. Unlike the nonetched solar cell, the reflectivity of b-Si solar cells increases in different levels after the Al_2O_3 passivation treatment on the wafer surface. A possible reason is that the ALD layers interfere with the original smooth gradient change of refractive index on the wafer surface generated by the b-Si structures. Another factor that would decrease the AR ability is that the deposited passivation layer does not fully cover the entire b-Si structure; hence, a

Table 2. Summary of Properties for the b-Si Solar Cells

etching time (min)	Al_2O_3 layer by ALD	efficiency (%)	FF	V_{oc} (V)	J_{sc} (mA/cm^2)	reflectivity
		HF:H_2O_2:H_2O in Volume 1:5:2				
2	before	7.08	0.59	0.566	21.2	*a*
	after	7.65	0.62	0.570	21.7	0.168
5	before	0.61	0.34	0.434	4.1	0.031
	after	1.09	0.49	0.458	4.9	0.063
10	before	0.42	0.42	0.430	2.3	0.030
	after	0.75	0.42	0.487	3.7	0.052
		HF:H_2O_2:H_2O in Volume 1:5:5				
2	before	6.54	0.63	0.573	18.1	0.225
	after	7.04	0.67	0.576	18.1	0.266
3	before	6.57	0.64	0.574	17.9	0.185
	after	7.35	0.68	0.576	18.8	0.257
4	before	6.32	0.56	0.572	19.9	*a*
	after	7.14	0.56	0.577	22.2	0.266
5	before	4.98	0.47	0.567	18.7	*a*
	after	5.62	0.52	0.575	18.6	0.234
10	before	1.34	0.33	0.464	8.6	0.011
	after	0.60	0.27	0.470	4.7	0.050
		HF:H_2O_2:H_2O in Volume 1:5:20				
2	before	4.77	0.55	0.562	15.5	*a*
	after	5.39	0.53	0.574	17.7	0.117
5	before	3.54	0.36	0.574	17.3	0.138
	after	4.86	0.45	0.576	18.6	0.177
10	before	2.97	0.31	0.532	17.7	*a*
	after	3.72	0.36	0.535	18.9	0.347
		HF:H_2O_2:H_2O in Volume 2:4:20				
2	before	4.47	0.48	0.570	16.4	0.106
	after	5.09	0.52	0.570	17.1	0.155
3	before	6.27	0.58	0.575	18.7	0.086
	after	7.34	0.73	0.574	17.4	0.141
4	before	7.03	0.67	0.554	18.9	0.079
	after	8.58	0.77	0.579	19.2	0.127
5	before	6.75	0.61	0.569	19.4	0.166
	after	6.91	0.63	0.568	19.3	0.229
		HF:H_2O_2:H_2O in Volume 3:3:20				
2	before	7.72	0.69	0.575	19.4	0.072
	after	8.47	0.77	0.579	19.1	0.143
3	before	8.35	0.75	0.588	19.0	0.064
	after	8.99	0.79	0.587	19.4	0.126
4	before	4.09	0.49	0.535	15.6	0.082
	after	5.43	0.54	0.572	17.5	0.146
5	before	3.76	0.38	0.545	18.1	0.077
	after	4.61	0.51	0.543	16.8	0.175
10	before	2.09	0.27	0.543	14.2	0.156
	after	2.53	0.30	0.554	15.2	0.217
		HF:H_2O_2:H_2O in Volume 4:2:20				
2	before	3.36	0.43	0.530	14.4	0.385
	after	4.26	0.45	0.575	16.6	0.235
3	before	5.86	0.57	0.574	17.8	*a*
	after	6.91	0.72	0.573	16.7	0.145
4	before	4.53	0.45	0.574	17.6	0.087
	after	5.36	0.55	0.574	17.1	0.156
5	before	3.06	0.37	0.543	15.2	0.087
	after	5.53	0.56	0.573	17.3	0.170

[a]Reflectivity not measured.

DOI: 10.1021/acsami.5b01008
ACS Appl. Mater. Interfaces 2015, 7, 11802−11814

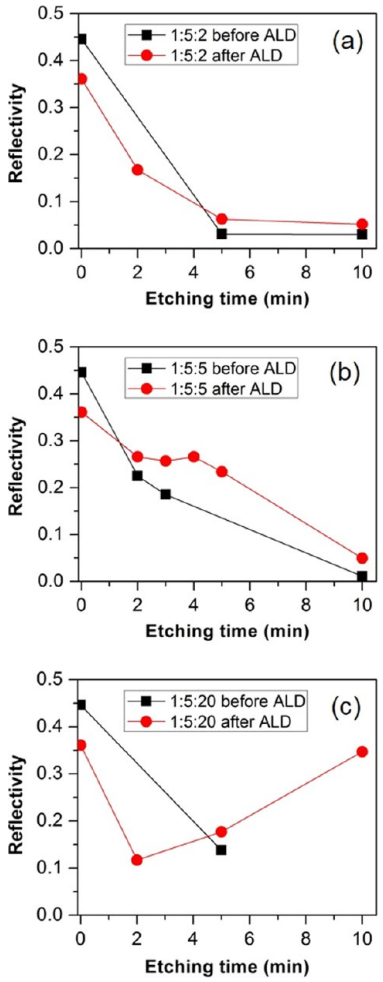

Figure 8. Plot of reflectivity for b-Si solar cells fabricated with the $HF:H_2O_2:H_2O$ ratio = 1:5:*Z* and various time before and after ALD. (a) $HF:H_2O_2:H_2O$ ratio = 1:5:2. (b) $HF:H_2O_2:H_2O$ ratio = 1:5:5. (c) $HF:H_2O_2:H_2O$ ratio = 1:5:20.

noncontinuous cover is formed on the wafer surface and causes a nonuniform gradient change of refractive index.

In general, the b-Si solar cells fabricated with the $HF:H_2O_2:H_2O$ ratio of 1:5:2 have lower reflectivity (Figure 8a) compared the cells fabricated with the ratio of 1:5:5 (Figure 8b) because the ones fabricated with the ratio of 1:5:2 usually have longer nanopores under the same etching time. The longer nanopores can provide smoother gradient changes of refractive index and more effectively suppress the reflectivity on the wafer surfaces. However, the uniformity of nanopore distribution on the wafer surfaces should be also taken into account since a more uniform distribution can also provide a smoother gradient change of refractive index. For example, after 5 min etching, the reflectivity of the solar cell fabricated with the 1:5:2 ratio after ALD, 0.063, is much lower than that of the one fabricated with the 1:5:5 ratio after ALD, 0.234. Although these two solar cells have similar nanopore distribution on the surface (Figures 5a and 6c), the former one possesses a lower reflectivity due to the much longer nanopores (950 nm versus 450 nm). After 10 min of etching, the b-Si solar cell fabricated with the 1:5:5 ratio has a longer nanopore length compared to that of the cell fabricated with the 1:5:2 ratio (850 nm versus 750 nm), but the reflectivities of both cells are almost the same after ALD (0.050 versus 0.052). This fact can be attributed to the observation that solar cells with short nanopores have a more uniform nanopore distribution.

On the basis of the same principle, the reflectivity should decrease with the etching time since the nanopores usually grow longer after longer etching times. This may explain the observation on the solar cells fabricated with the ratios of 1:5:2 and 1:5:5 for various time. However, the solar cells fabricated with the ratio 1:5:20 show the opposite trend, which is that the surface reflectivity increases with etching time (Figure 8c). A possible explanation is that, after longer etching, some regions of b-Si structures become extremely porous and collapse like samples etched with the other etchant ratios. Since the nanopore growth rate with the 1:5:20 ratio is much slower compared to those from the other etchant ratios, the positive effect that the nanopore growth brings, smoothing the gradient change of refractive index, is not able to compensate for the negative effect that the structure collapse brings, destroying the gradient change of refractive index. Hence, the change of refractive index becomes discrete which causes the Si wafer reflectivity to increase with etching time.

The morphology of b-Si has a significant impact on not only the surface reflectivity but also the energy conversion efficiency of the b-Si solar cells. Figure 9 shows a plot of the efficiency of b-

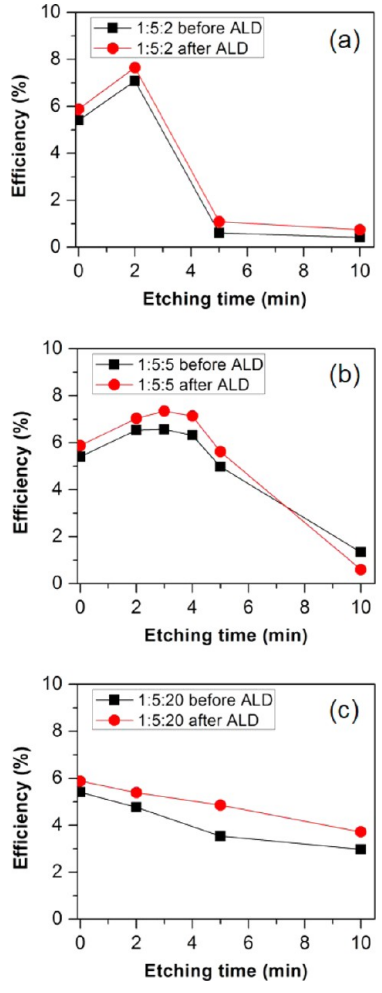

Figure 9. Plot of efficiency for b-Si solar cells fabricated with the $HF:H_2O_2:H_2O$ ratio = 1:5:*Z* and various etching time before and after ALD. (a) $HF:H_2O_2:H_2O$ ratio = 1:5:2. (b) $HF:H_2O_2:H_2O$ ratio = 1:5:5. (c) $HF:H_2O_2:H_2O$ ratio = 1:5:20.

DOI: 10.1021/acsami.5b01008
ACS Appl. Mater. Interfaces 2015, 7, 11802−11814

Si solar cells fabricated with the ratio of 1:5:*Z*. In general, the solar cell efficiency decreases with etching time, even though most of the cells have lower reflectivity after longer etching because the carrier recombination rate is also increased after the longer etching. During the etching, the nanopore length increases with time which causes the b-Si to become more porous and increases the surface areas of the b-Si structure with time as well. With the larger surface area, more dangling bonds are shown on the wafer surface leading to a higher surface recombination velocity of the carriers and a decrease in the solar cell efficiency.

With the Si etchant consisting of $HF:H_2O_2:H_2O$ = 1:5:2, the b-Si solar cells have the highest efficiency after 2 min of etching, 7.65% after ALD (Figure 9a), compared to the two other etchant compositions. This is most likely due to the relatively longer nanopore length. However, after 5 min of etching, the efficiency decreased to 1.09% after ALD. Although the increase in the nanopore surface area might be one of the factors resulting from this situation, the damage of the p−n junction interface should be considered a main reason for the decrease in efficiency. The nanopore length reaches 950 nm, which is long enough to penetrate the p−n junction interface and worsen the solar cell functionality. The V_{oc} and J_{sc} drop from 0.566 to 0.434 V and 21.2 to 4.2 mA/cm^2 before ALD, respectively, indicating the excessively long nanopores have deteriorated the energy conversion ability of solar cell.

The b-Si solar cells fabricated with the ratio of 1:5:5 show a slightly different trend of efficiency (Figure 9b) compared to the cells fabricated with the ratio of 1:5:2. The solar cell efficiency slightly increases during the early stage of etching and reaches the maximum, 7.35%, after 3 min of etching and then starts to decrease. The small increase of efficiency results from the small decrease of reflectivity on the wafer surface. After that stage, due to the increased growth of nanopore length creating larger surface areas, the solar cell efficiency also drops similarly to the cells fabricated with the 1:5:2 ratio but with a slower rate. The slower drop of efficiency can be attributed to the lower growth rate of the nanopores. It is reasonable to infer that the nanopores also penetrate the p−n junction interface after 10 min of etching since the J_{sc} and V_{oc} decrease from 18.70 to 8.65 mA/cm^2 and 0.567 to 0.464 V before ALD, respectively. One thing that needs to be mentioned is that, after etching for 10 min, the efficiency after ALD is lower than the efficiency before ALD because some parts of the Al back contact fell off the Si wafer back surface during ALD which would increase the back contact resistance.

Compared to the b-Si solar cells etched with the 1:5:2 and 1:5:5 ratio, the V_{oc} of solar cells fabricated with the 1:5:20 ratio does not dramatically drop with etching (Figure 9c) since the nanopores are not long enough to penetrate the interface of the p−n junction. However, the efficiency still decreases with etching time because of the significant increase in reflectivity. This fact once again indicates that not only the reflectivity but also the b-Si morphology affect the energy conversion efficiency of b-Si solar cells.

3.4. Effects of $HF:H_2O_2$ Ratio on b-Si Solar Cell Fabrication. It has been shown that using lower [HF] and [H_2O_2] (i.e., $HF:H_2O_2:H_2O$ = 1:5:20) prevents the fabricated nanopores penetrating the p−n junction interface. Hence, the solar cells fabricated with low [HF] and [H_2O_2] (i.e., $HF:H_2O_2:H_2O$ = *X*:*Y*:20) have been systematically investigated in order to better understand how the relative ratio of $HF:H_2O_2$ affects the morphology and other properties of b-Si solar cells. Figure 10 shows the SEM images of b-Si solar cells etched with various $HF:H_2O_2:H_2O$ volume ratios for 3 min. With $HF:H_2O_2:H_2O$ = 2:4:20 and 3 min of etching, the fabricated nanopores in the b-Si solar cell have maximum diameter of 40 nm. The maximum nanopore length is only 130 nm (Figure 10a,b), which is much shorter than that of the nanopores fabricated with the 1:5:5 ratio for 3 min (240 nm, Figure 7b). This is not surprising since both [HF] and [H_2O_2] in the 2:4:20 ratio etch are lower than that using the 1:5:5 ratio. However, the nanopore length of b-Si fabricated with the 2:4:20 ratio for 3 min of etching (130 nm) is longer than that fabricated with the 1:5:20 ratio for 5 min (100 nm). This fact proves that the relative ratio of HF to H_2O_2 is indeed directly related to the b-Si morphology during the etching.

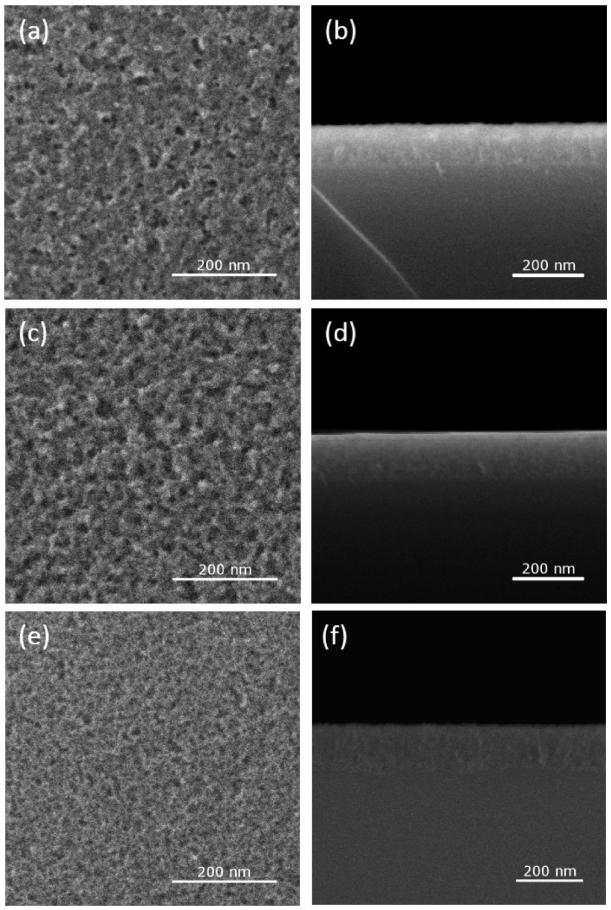

Figure 10. Surface and cross-sectional SEM images of b-Si solar cell fabricated for 3 min with a $HF:H_2O_2:H_2O$ volume ratio equal to 2:4:20 (a, b), 3:3:20 (c, d), and 4:2:20 (e, f).

As the $HF:H_2O_2$ relative ratio increases to 3:3 (i.e., $HF:H_2O_2:H_2O$ ratio = 3:3:20), the maximum diameter and length of nanopores slightly increase from 40 to 45 nm and 130 to 150 nm, respectively (Figure 10c,d). In addition, the number of nanopores on the wafer surface increases and the nanopore distribution is more uniform on the wafer surface as well (Figure 10c,d). A possible explanation is that the higher $HF:H_2O_2$ relative ratio allows more HF molecules to immediately etch the as-formed SiO_2 on the wafer surface, so that the size and number of nanopores would increase. However, once the $HF:H_2O_2$ ratio further increases to 4:2 (the $HF:H_2O_2:H_2O$ ratio = 4:2:20), the nanopore number on the wafer surface starts to decrease rather than continue to increase. The nanopore diameter and length also slightly decrease to 30 and 140 nm,

DOI: 10.1021/acsami.5b01008
ACS Appl. Mater. Interfaces 2015, 7, 11802−11814

respectively (Figure 10e, f), because the lower $[H_2O_2]$ in the etchant provides a lower oxidization rate of Si, which is not favorable for the nanopore formation even though [HF] is higher.

The etching time also has a significant impact on the b-Si morphology of Si solar cells fabricated with the $HF:H_2O_2:H_2O = X:Y:20$. Here the b-Si solar cells fabricated with the ratio of 3:3:20 are the focus since they have the longest nanopores and the most uniform nanopore distribution compared to the cells fabricated with the other *X*:*Y*:20 ratios. SEM images of b-Si fabricated with $HF:H_2O_2:H_2O$ = 3:3:20 for variant etching time are shown in Figures 11 and 12.

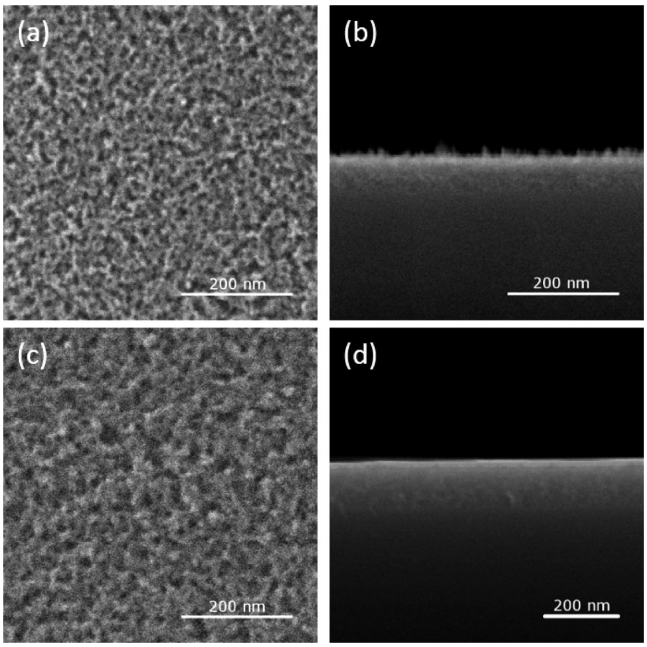

Figure 11. Surface and cross-sectional SEM images of a b-Si solar cell fabricated with a $HF:H_2O_2:H_2O$ volume ratio = 3:3:20 for 2 min (a, b) and 3 min (c, d).

After 2 min of etching, the Si wafer surface possesses a high population density of nanopores, and these nanopores are uniformly distributed on the wafer surface with the maximum diameter of 30 nm and length of 130 nm (Figure 11a,b). It can also be seen that some nonetched regions of Si wafer surface turn into the small and short Si pillars standing on the wafer surface. After etching for 3 min, the small Si pillars disappear, and only nanopores exist on the wafer surface leaving a relatively smooth surface (Figure 11c,d). The maximum diameter and length of the nanopores slightly increase to 45 and 150 nm, respectively. From the cross-sectional SEM image, the continuous change of brightness on the b-Si structure indicates that the Si surface porosity changes with depth, or the refractive index of Si changes with depth, which is more beneficial for suppressing reflectivity on the wafer surface (Figure 11d). The difference in height between the Au−Si interface and b-Si top surface is around 15 nm (Supporting Information Figure S4). The Au contact is thinner than 100 nm because some parts of the contact collapse during the wafer cutting for the SEM image.

When the etching time increases from 3 to 5 min, the nanopores have maximum diameter and length of 55 and 190 nm, respectively (Figure 12a,b). The collapse of the b-Si structure starts being observed and makes the number of

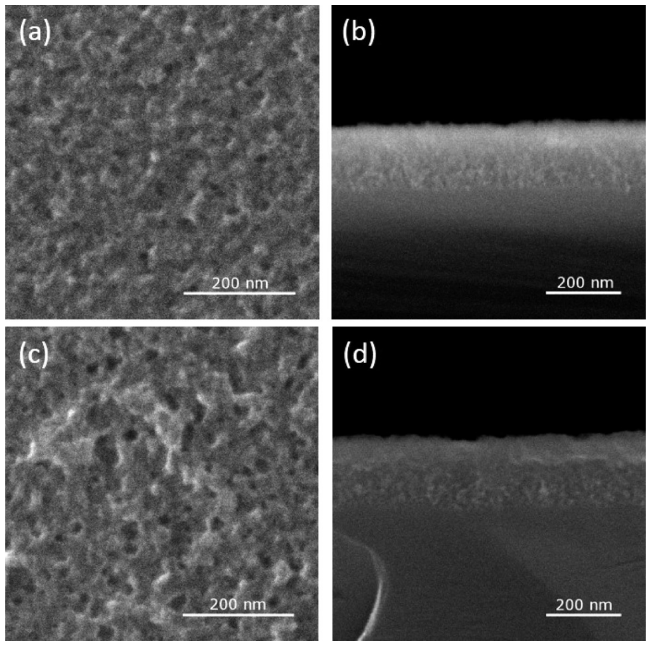

Figure 12. Surface and cross-sectional SEM images of b-Si solar cell fabricated with a $HF:H_2O_2:H_2O$ volume ratio = 3:3:20 for 5 min (a, b) and 10 min (c, d).

nanopores decrease and the wafer surface rugged, characteristics which are detrimental to the AR ability of the b-Si structure. As the etching time further increases to 10 min, the maximum nanopore diameter and length increase to 70 and 220 nm, respectively (Figure 12c,d). The Si wafer surface becomes more rugged, and the b-Si structure collapses further, leading to a higher reflectivity because of the less smooth gradient change of the refractive index. In a comparison of the b-Si solar cells fabricated with the 3:3:20 ratio to those fabricated with the 1:5:20 ratio, it can be found that the former cells possess much longer nanopores (e.g., 190 nm versus 100 nm after 5 min etching). This result indicates that the 3:3:20 ratio indeed provides a higher Si etching rate (a faster nanopore growth rate) compared with the other etchant compositions.

Similar to the b-Si solar cells fabricated with $HF:H_2O_2:H_2O = 1:5:Z$, the reflectivity of solar cells fabricated with the *X*:*Y*:20 ratios has strong dependence on the b-Si morphology. Nevertheless, the reflectivities of solar cells fabricated with the *X*:*Y*:20 ratio are generally higher due to their shorter nanopores. A plot of the reflectivity of b-Si solar cells fabricated with the ratio of X:Y:20 is shown in Figure 13.

In addition, like the solar cells fabricated with $HF:H_2O_2:H_2O = 1:5:Z$, the surface reflectivity of cells fabricated with the *X*:*Y*:20 ratios also increases after the ALD passivation treatment. The reason is that the Al_2O_3 passivation layer brings another refractive index on the b-Si surface which interferes with the original gradient change of refractive index with the b-Si. Figure 14 shows reflectivity spectra of nonetched solar cells and b-Si solar cells. This change of the refractive index within the b-Si structure not only affects the reflectivity of cell surface but also leads to the shift of peaks on the reflectivity curves (Figure 14c,d).

As discussed above, the reflectivity of solar cells fabricated with the ratio of 1:5:20 increases with the etching time (Figure 13a) because the slow b-Si growth cannot compensate for the negative effect on reflectivity resulting from the b-Si collapse during

DOI: 10.1021/acsami.5b01008
ACS Appl. Mater. Interfaces 2015, 7, 11802−11814

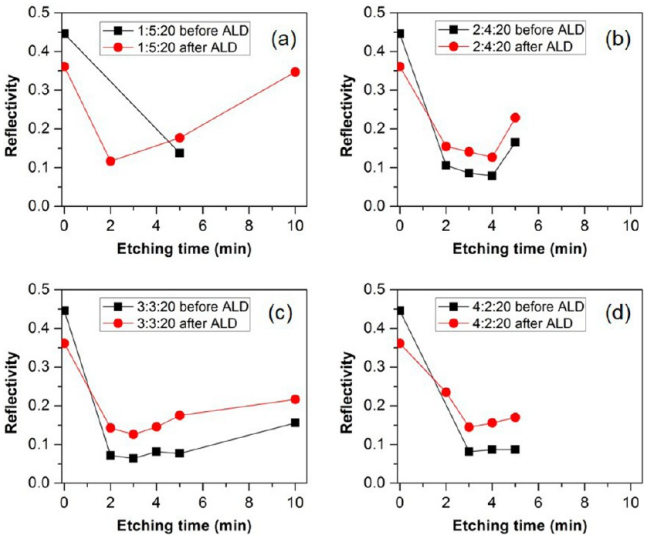

Figure 13. Plot of reflectivity for b-Si solar cells fabricated with the $HF:H_2O_2:H_2O$ ratio = *X*:*Y*:20 and various time before and after ALD. (a) $HF:H_2O_2:H_2O$ ratio = 1:5:20. (b) $HF:H_2O_2:H_2O$ ratio = 2:4:20. (c) $HF:H_2O_2:H_2O$ ratio = 3:3:20. (d) $HF:H_2O_2:H_2O$ ratio = 4:2:20.

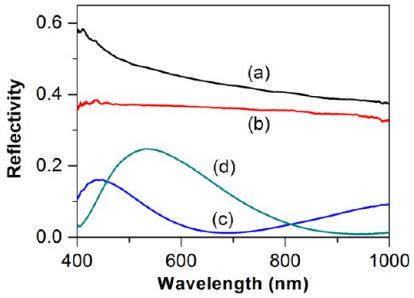

Figure 14. Reflectivity spectra of nonetched Si solar cell and b-Si solar cell fabricated with the ratio 3:3:20 for 3 min before and after ALD. (a) Nonetched Si solar cell before ALD. (b) Nonetched Si solar cell after ALD. (c) $HF:H_2O_2:H_2O$ ratio = 3:3:20 before ALD. (d) $HF:H_2O_2:H_2O$ ratio = 3:3:20 after ALD.

etching. Unlike the b-Si solar cells fabricated with the ratio of 1:5:20, the cells fabricated with the ratios of 2:4:20, 3:3:20, and 4:2:20 possess a slightly different trend of reflectivity, which slightly decreases with the etching time first and then increases (Figure 13b–d). However, the concept used to explain the reflectivity trend of surfaces fabricated with the 1:5:20 ratio can also be used to explain this observation. During the early stage of etching, only nanopores are produced on the Si wafer surface leading to a lower surface reflectivity. After a time, some top parts of b-Si structures become more porous and start to collapse, destroying the gradient change of the refractive index. However, as the nanopores are continuing to grow, the overall reflectivity can keep decreasing and reach the minimum as long as the collapse has not yet become too great. Nevertheless, once the collapse becomes significant, the collapse would dominate the change of reflectivity and lead to an increase in the surface reflectivity.

Since the relative ratios of HF to H_2O_2 in the $HF:H_2O_2:H_2O$ ratios of 2:4:20, 3:3:20, and 4:2:20 are closer to 1 compared to the relative ratio in the 1:5:20 ratio, the nanopore growth rates from the former etchant compositions are faster than that of the latter composition because HF and H_2O_2 in the etchants are both sufficient to grow longer nanopores. Hence, the collapse of b-Si structure of the solar cells fabricated with the former etchant compositions (the 2:4:20, 3:3:20, and 4:2:20 ratios) has less domination on the reflectivity, which allows the solar cell reflectivity to reach the maximum first and then increase. Among all the solar cells fabricated with the ratio *X*:*Y*:20, the cell fabricated with the 3:3:20 ratio possesses the lowest reflectivity after 3 min etching, 12.6%, because of the faster etching rate, or the longer nanopore length.

Unlike the b-Si solar cells fabricated with the $HF:H_2O_2:H_2O$ ratios of 1:5:2 and 1:5:5, the cells fabricated with the ratios *X*:*Y*:20 show a more stable energy conversion efficiency with etching time. Also, the V_{oc} does not drop after a longer time as well because of the slower nanopore growth rate. The slower growth rate can prevent the nanopores from growing too long and destroying the interface of the p–n junctions. A plot of the efficiency of b-Si solar cells etched with the ratio of *X*:*Y*:20 is shown in Figure 15.

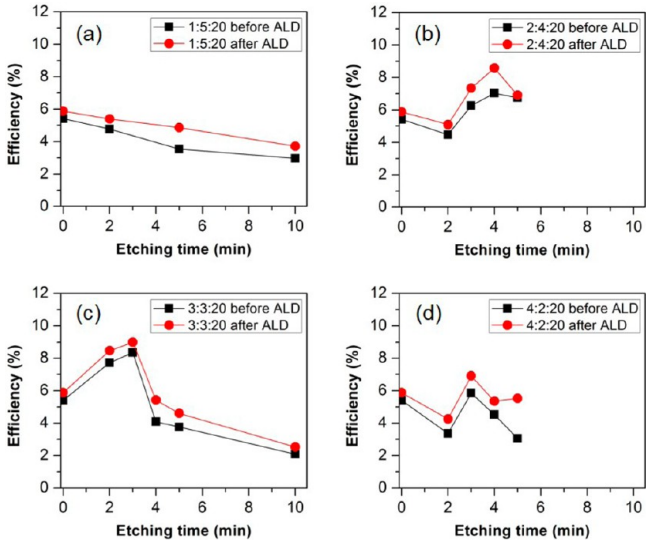

Figure 15. Plot of efficiency for b-Si solar cells fabricated with the $HF:H_2O_2:H_2O$ ratio = *X*:*Y*:20 and various time before and after ALD. (a) $HF:H_2O_2:H_2O$ ratio = 1:5:20. (b) $HF:H_2O_2:H_2O$ ratio = 2:4:20. (c) $HF:H_2O_2:H_2O$ ratio = 3:3:20. (d) $HF:H_2O_2:H_2O$ ratio = 4:2:20.

As mentioned before, when the etchant with $HF:H_2O_2:H_2O$ ratio as 1:5:20 is used, the solar cell efficiency decreases with etching time because of the higher surface reflectivity that results from the relatively large collapse of nanopores (Figure 15a). For the solar cells fabricated with the ratios 2:4:20, 3:3:20, and 4:2:20, the solar cell efficiency increases with the etching time first and then decreases after reaching the maximum (Figure 15b–d), which is opposite to the trend of reflectivity. The efficiency increases at the early state of etching because the growing nanopores can effectively suppress the reflectivity by providing a smoother gradient change of refractive index. However, once the collapse of nanopores starts, the gradient charge of refractive index is interrupted which would increase the reflectivity and decrease the efficiency. Nevertheless, the increase in surface area of nanopores after the longer etching time might also explain the decrease in efficiency, since the larger surface area would increase the surface recombination velocity.

Among these different etchant compositions, the b-Si solar cells fabricated with the 3:3:20 ratio shows the highest efficiency. The highest efficiency of the solar cell fabricated with 3:3:20 ratio after ALD is 8.99%, which is much higher than the efficiency of

DOI: 10.1021/acsami.5b01008
ACS Appl. Mater. Interfaces 2015, 7, 11802–11814

cells fabricated with the 2:4:20 ratio and 4:2:20 ratio, 8.58% and 6.91%, respectively. The reason is that the cell fabricated with the 3:3:20 ratio can provide a longer nanopore length and a more uniform distribution of nanopores on the wafer surface (Figure 10); both of these two properties are beneficial for improving the AR ability of Si wafer surface.

The high fill factor (FF) of a b-Si solar cell fabricated with the 3:3:20 ratio also indicates that the Au contacts adhere well to the wafer surface during the early stage of the etching process. Figure 16 shows a plot of $I-V$ curves of the nonetched Si solar cell and

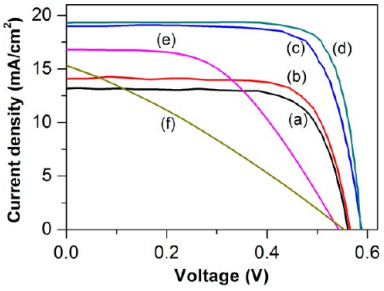

Figure 16. Plot of $I-V$ curves of nonetched Si solar cell and b-Si solar cells fabricated with the HF:H_2O_2:H_2O ratio = 3:3:20 and various time before and after ALD. (a) Nonetched Si solar cell before ALD. (b) Nonetched Si solar cell after ALD. (c) Si solar cell etched for 3 min before ALD. (d) Si solar cell etched for 3 min after ALD. (e) Si solar cell etched for 5 min after ALD. (f) Si solar cell etched for 10 min after ALD.

b-Si solar cell fabricated with the 3:3:20 ratio. Before etching, the nonetched Si solar cell has a high FF, 0.73, which is slightly improved to 0.74 after the Al_2O_3 passivation treatment by ALD. After 3 min of etching, the FF of b-Si solar cell becomes higher, which is 0.75 and 0.79 before and after ALD, respectively. Also, compared to the nonetched solar cell, the cell etched for 3 min shows an improved V_{oc} due to suppression of Auger recombination which might indicate the existence of a SE in the Si solar cell. However, after 5 min and 10 min of etching, the FF dramatically decreases to 0.51 and 0.30 after ALD, respectively, and the efficiency also drops to 4.61% and 2.53%, respectively. This result shows that, as the etching time increases, the adhesion between the Au contacts and the wafer surface becomes worse causing a higher resistance between the contact and the wafer, or a lower FF and efficiency of the cells.

4. CONCLUSIONS

We have demonstrated the first example of Au top contacts rather than metal NPs or chemicals being the catalysts for fabrication of b-Si AR layers on Si solar cells by using the CACE method. Thus, the b-Si AR layers are easily fabricated on the cell surfaces without addition and removal of any metal catalyst. The Au contacts catalyze the Si etching and can adhere well to the cell surface during the etching process. The fabricated Si solar cells not only suppress the surface reflectivity to absorb more incident light by the b-Si AR layers, but also more effectively collect electrons to improve the V_{oc} and J_{sc} of solar cells by the SEs. The Si solar cell fabricated with the etchant consisting of the HF:H_2O_2:H_2O ratio = 3:3:20 has the highest efficiency among all the samples, 8.99%, with the b-Si AR layer thickness of 150 nm, after 3 min of etching. The SEM analysis indicates that the b-Si structures will collapse after a longer etching time. Correlated with the trends in efficiency and reflectivity, this collapse has a detrimental effect on the reflectivity and energy conversion efficiency.

The CACE method involves a novel concept: a component in an electronic device (i.e., the Au top contacts) can also function as a catalyst in a chemical reaction to generate a new functional structure in the device. The CACE method is simple enough to be adapted to the current production lines of Si solar cells since there is no complicated step involved in the method. Compared to the current fabrication processes of b-Si solar cells based on the MACE method, the CACE method requires fewer operation steps and is more beneficial for the Si solar cell industry to further cut down the cost of per watt output of Si solar cells.

■ ASSOCIATED CONTENT

Supporting Information

Tables of metal content in the chemicals, summary of the Si etchants, diagram of the mask for sputtering of Au contacts, and comparison of the MACE and CACE processes. The Supporting Information is available free of charge on the ACS Publications website at DOI: 10.1021/acsami.5b01008.

■ AUTHOR INFORMATION

Corresponding Author

*E-mail: arb@rice.edu. Phone: +1 713 348 5610.

Notes

The authors declare the following competing financial interest(s): These studies were supported in part by funding from Natcore Technology, Inc. This author is the scientific founder of, and has an equity interest in, Natcore Technology, Inc., a publically traded company (NXT.V) that may potentially benefit from the research results.

■ ACKNOWLEDGMENTS

This work was supported by the Robert A. Welch Foundation (C-0002), the Welsh Government Ser Cymru Programme, and in part by Natcore Technology, Inc. (NXT.V). We are grateful to D. J. Flood and D. H. Levy for useful discussion and for assistance with ALD. A.R.B. is the scientific founder of, and has an equity interest in, Natcore Technology, Inc., a publically traded company (NXT.V) that may potentially benefit from the research results.

■ REFERENCES

(1) Barron, A. R. Cost Reduction in the Solar Industry. *Mater. Today* **2014**, *18*, 2−3.

(2) Walheim, S.; Schaffer, E.; Mlynek, J.; Steiner, U. Nanophase-Separated Polymer Films as High-Performance Antireflection Coatings. *Science* **1999**, *283*, 520−522.

(3) Wu, C.; Crouch, C. H.; Zhao, L.; Carey, J. E.; Younkin, R.; Levinson, J. A.; Mazur, E.; Farrell, R. M.; Gothoskar, P.; Karger, A. Near-Unity Below-Band-Gap Absorption by Microstructured Silicon. *Appl. Phys. Lett.* **2001**, *78*, 1850−1852.

(4) Ma, L. L.; Zhou, Y. C.; Jiang, N.; Lu, X.; Shao, J.; Lu, W.; Ge, J.; Ding, X. M.; Hou, X. Y. Wide-Band "Black Silicon" Based on Porous Silicon. *Appl. Phys. Lett.* **2006**, *88*, 171907.

(5) Kuo, M. L.; Poxson, D. J.; Kim, Y. S.; Mont, F. W.; Kim, L. K.; Schuhert, E. F.; Lin, S. Y. Realization of a Near-Perfect Antireflection Coating for Silicon Solar Energy Utilization. *Opt. Lett.* **2008**, *33*, 2527−2529.

(6) Huang, Y.-F.; Chattopadhyay, S.; Jen, Y.-J.; Peng, C.-Y.; Liu, T.-A.; Hsu, Y.-K.; Pan, C.-L.; Lo, H.-C.; Hsu, C.-H.; Chang, Y.-H.; Lee, C.-S.; Chen, K.-H.; Chen, L.-C. Improved Broadband and Quasi-Omnidirectional Anti-Reflection Properties with Biomimetic Silicon Nanostructures. *Nat. Nanotechnol.* **2007**, *2*, 770−774.

(7) Jansen, H.; Deboer, M.; Legtenberg, R.; Elwenspoek, M. The Black Silicon Method - a Universal Method for Determining the Parameter

DOI: 10.1021/acsami.5b01008
ACS Appl. Mater. Interfaces 2015, 7, 11802−11814

Setting of a Fluorine-Based Reactive Ion Etcher in Deep Silicon Trench Etching with Profile Control. *J. Micromech. Microeng.* **1995**, *5*, 115−120.
(8) Hirai, Y.; Yabu, H.; Matsuo, Y.; Ijiro, K.; Shimomura, M. Biomimetic Bi-Functional Silicon Nanospike-Array Structures Prepared by Using Self-Organized Honeycomb Templates and Reactive Ion Etching. *J. Mater. Chem.* **2010**, *20*, 10804−10808.
(9) Sun, G.; Gao, T.; Zhao, X.; Zhang, H. Fabrication of Micro/Nano Dual-Scale Structures by Improved Deep Reactive Ion Etching. *J. Micromech. Microeng.* **2010**, *20*, 075028.
(10) Lee, K.; Ha, M.-H.; Kim, J. H.; Jeong, J.-W. Damage-Free Reactive Ion Etch for High-Efficiency Large-Area Multi-Crystalline Silicon Solar Cells. *Sol. Energy Mater. Sol. Cells* **2011**, *95*, 66−68.
(11) Yoo, J.; Yu, G.; Yi, J. Large-Area Multicrystalline Silicon Solar Cell Fabrication Using Reactive Ion Etching (RIE). *Sol. Energy Mater. Sol. Cells* **2011**, *95*, 2−6.
(12) Jansen, H. V.; de Boer, M. J.; Unnikrishnan, S.; Louwerse, M. C.; Elwenspoek, M. C. Black Silicon Method X: a Review on High Speed and Selective Plasma Etching of Silicon with Profile Control: an In-Depth Comparison Between Bosch and Cryostat DRIE Processes as a Roadmap to Next Generation Equipment. *J. Micromech. Microeng.* **2009**, *19*, 033001.
(13) Dussart, R.; Tillocher, T.; Lefaucheux, P.; Boufnichel, M. Plasma Cryogenic Etching of Silicon: from the Early Days to Today's Advanced Technologies. *J. Phys. D: Appl. Phys.* **2014**, *47*, 123001.
(14) Her, T. H.; Finlay, R. J.; Wu, C.; Deliwala, S.; Mazur, E. Microstructuring of Silicon with Femtosecond Laser Pulses. *Appl. Phys. Lett.* **1998**, *73*, 1673−1675.
(15) Younkin, R.; Carey, J. E.; Mazur, E.; Levinson, J. A.; Friend, C. M. Infrared Absorption by Conical Silicon Microstructures Made in a Variety of Background Gases Using Femtosecond-Laser Pulses. *J. Appl. Phys.* **2003**, *93*, 2626−2629.
(16) Radu, C.; Simion, S.; Zamfirescu, M.; Ulmeanu, M.; Enculescu, M.; Radoiu, M. Silicon Structuring by Etching with Liquid Chlorine and Fluorine Precursors Using Femtosecond Laser Pulses. *J. Appl. Phys.* **2011**, *110*, 034901.
(17) Crouch, C. H.; Carey, J. E.; Warrender, J. M.; Aziz, M. J.; Mazur, E.; Génin, F. Y. Comparison of Structure and Properties of Femtosecond and Nanosecond Laser-Structured Silicon. *Appl. Phys. Lett.* **2004**, *84*, 1850−1852.
(18) Halbwax, M.; Sarnet, T.; Delaporte, P.; Sentis, M.; Etienne, H.; Torregrosa, F.; Vervisch, V.; Perichaud, I.; Martinuzzi, S. Micro and Nano-Structuration of Silicon by Femtosecond Laser: Application to Silicon Photovoltaic Cells Fabrication. *Thin Solid Films* **2008**, *516*, 6791−6795.
(19) Canham, L. T. Silicon Quantum Wire Array Fabrication by Electrochemical and Chemical Dissolution of Wafers. *Appl. Phys. Lett.* **1990**, *57*, 1046−1048.
(20) Lv, H.; Shen, H.; Jiang, Y.; Gao, C.; Zhao, H.; Yuan, J. Porous-Pyramids Structured Silicon Surface with Low Reflectance over a Broad Band by Electrochemical Etching. *Appl. Surf. Sci.* **2012**, *258*, 5451−5454.
(21) Zhang, X. G. Morphology and Formation Mechanisms of Porous Silicon. *J. Electrochem. Soc.* **2004**, *151*, C69.
(22) Striemer, C. C.; Fauchet, P. M. Dynamic Etching of Silicon for Broadband Antireflection Applications. *Appl. Phys. Lett.* **2002**, *81*, 2980−2982.
(23) Chattopadhyay, S.; Huang, Y. F.; Jen, Y. J.; Ganguly, A.; Chen, K. H.; Chen, L. C. Anti-Reflecting and Photonic Nanostructures. *Mater. Sci. Eng., R* **2010**, *69*, 1−35.
(24) Hsu, C.-H.; Wu, J.-R.; Lu, Y.-T.; Flood, D. J.; Barron, A. R.; Chen, L.-C. Fabrication and Characteristics of Black Silicon for Solar Cell Applications: an Overview. *Mater. Sci. Semicond. Process.* **2014**, *25*, 2−17.
(25) Huang, Z.; Geyer, N.; Werner, P.; de Boor, J.; Gösele, U. Metal-Assisted Chemical Etching of Silicon: a Review. *Adv. Mater.* **2011**, *23*, 285−308.
(26) Branz, H. M.; Yost, V. E.; Ward, S.; Jones, K. M.; To, B.; Stradins, P. Nanostructured Black Silicon and the Optical Reflectance of Graded-Density Surfaces. *Appl. Phys. Lett.* **2009**, *94*, 231121.
(27) Mikhael, B.; Elise, B.; Xavier, M.; Sebastian, S.; Johann, M.; Laetitia, P. New Silicon Architectures by Gold-Assisted Chemical Etching. *ACS Appl. Mater. Interfaces* **2011**, *3*, 3866−3873.
(28) Oh, J.; Yuan, H.-C.; Branz, H. M. An 18.2%-Efficient Black-Silicon Solar Cell Achieved through Control of Carrier Recombination in Nanostructures. *Nat. Nanotechnol.* **2012**, *7*, 743−748.
(29) Lu, Y.-T.; Barron, A. R. Nanopore-Type Black Silicon Anti-Reflection Layers Fabricated by a One-Step Silver-Assisted Chemical Etching. *Phys. Chem. Chem. Phys.* **2013**, *15*, 9862−9870.
(30) Srivastava, S. K.; Kumar, D.; Sharma, M.; Kumar, R.; Singh, P. K. Silver Catalyzed Nano-Texturing of Silicon Surfaces for Solar Cell Applications. *Sol. Energy Mater. Sol. Cells* **2012**, *100*, 33−38.
(31) Geng, X.; Qi, Z.; Li, M.; Duan, B. K.; Zhao, L.; Bohn, P. W. Fabrication of Antireflective Layers on Silicon Using Metal-Assisted Chemical Etching with In Situ Deposition of Silver Nanoparticle Catalysts. *Sol. Energy Mater. Sol. Cells* **2012**, *103*, 98−107.
(32) Peng, K.; Wang, X.; Lee, S.-T. Silicon Nanowire Array Photoelectrochemical Solar Cells. *Appl. Phys. Lett.* **2008**, *92*, 163103.
(33) Lu, Y.-T.; Barron, A. R. Anti-Reflection Layers Fabricated by a One-Step Copper-Assisted Chemical Etching with Inverted Pyramidal Structures Intermediate between Texturing and Nanopore-Type Black Silicon. *J. Mater. Chem. A* **2014**, *2*, 12043−12052.
(34) Koynov, S.; Brandt, M. S.; Stutzmann, M. Black Nonreflecting Silicon Surfaces for Solar Cells. *Appl. Phys. Lett.* **2006**, *88*, 203107.
(35) Xiu, Y.; Zhang, S.; Yelundur, V.; Rohatgi, A.; Hess, D. W.; Wong, C. P. Superhydrophobic and Low Light Reflectivity Silicon Surfaces Fabricated by Hierarchical Etching. *Langmuir* **2008**, *24*, 10421−10426.
(36) Song, K.; Kim, B.; Lee, H.; Lee, Y.-J.; Park, C.; Balaji, N.; Ju, M.; Choi, J.; Yi, J. Selective Emitter Using a Screen Printed Etch Barrier in Crystalline Silicon Solar Cell. *Nanoscale Res. Lett.* **2012**, *7*, 410.
(37) Liang, Z.; Zeng, F.; Song, H.; Shen, H. Effect of Porous Si and an Etch-Back Process on the Performance of a Selective Emitter Solar Cell. *Sol. Energy Mater. Sol. Cells* **2013**, *109*, 26−30.
(38) Zhu, L. Q.; Gong, J.; Huang, J.; She, P.; Zeng, M. L.; Li, L.; Dai, M. Z.; Wan, Q. Improving the Efficiency of Crystalline Silicon Solar Cells by an Intersected Selective Laser Doping. *Sol. Energy Mater. Sol. Cells* **2011**, *95*, 3347−3351.
(39) Wang, K. S.; Tjahjono, B. S.; Wong, J.; Uddin, A.; Wenham, S. R. Sheet Resistance Characterization of Laser-Doped Lines on Crystalline Silicon Wafers for Photovoltaic Applications. *Sol. Energy Mater. Sol. Cells* **2011**, *95*, 974−980.
(40) Wang, S.; Lennon, A.; Tjahjono, B.; Mai, L.; Vogl, B.; Wenham, S. Overcoming Over-Plating Problems for PECVD SiN_x Passivated Laser Doped p-Type Multi-Crystalline Silicon Solar Cells. *Sol. Energy Mater. Sol. Cells* **2012**, *99*, 226−230.
(41) Jeon, M.; Lee, J.; Kim, S.; Lee, W.; Cho, E. Ion Implanted Crystalline Silicon Solar Cells with Blanket and Selective Emitter. *Mater. Sci. Eng., B* **2011**, *176*, 1285−1290.
(42) Lee, C.-M.; Chang, S.-P.; Chang, S.-J.; Wu, C.-I. p-Type Quasi-Mono Silicon Solar Cell Fabricated by Ion Implantation. *Int. J. Photoenergy* **2013**, *2013*, 171390.
(43) Lee, E.; Cho, K.; Oh, D.; Shim, J.; Lee, H.; Choi, J.; Kim, J.; Shin, J.; Lee, S.; Lee, H. Exceeding 19% Efficient 6 Inch Screen Printed Crystalline Silicon Solar Cells with Selective Emitter. *Renewable Energy* **2012**, *42*, 95−98.
(44) Uzum, A.; Hamdi, A.; Nagashima, S.; Suzuki, S.; Suzuki, H.; Yoshiba, S.; Dhamrin, M.; Kamisako, K.; Sato, H.; Katsuma, K.; Kato, K. Selective Emitter Formation Process Using Single Screen-Printed Phosphorus Diffusion Source. *Sol. Energy Mater. Sol. Cells* **2013**, *109*, 288−293.
(45) Um, H.-D.; Park, K.-T.; Jung, J.-Y.; Li, X.; Zhou, K.; Jee, S.-W.; Lee, J.-H. Incorporation of a Self-Aligned Selective Emitter to Realize Highly Efficient (12.8%) Si Nanowire Solar Cells. *Nanoscale* **2014**, *6*, 5193−5199.
(46) Lianto, P.; Yu, S.; Wu, J.; Thompson, C. V.; Choi, W. K. Vertical Etching with Isolated Catalysts in Metal-Assisted Chemical Etching of Silicon. *Nanoscale* **2012**, *4*, 7532−7539.
(47) Li, L.; Zhao, X.; Wong, C.-P. Deep Etching of Single- and Polycrystalline Silicon with High Speed, High Aspect Ratio, High

DOI: 10.1021/acsami.5b01008
ACS Appl. Mater. Interfaces 2015, 7, 11802−11814

Uniformity, and 3D Complexity by Electric Bias-Attenuated Metal-Assisted Chemical Etching (EMaCE). *ACS Appl. Mater. Interfaces* **2014**, *6*, 16782−16791.

DOI: 10.1021/acsami.5b01008
ACS Appl. Mater. Interfaces 2015, 7, 11802−11814